




Chiral spin liquid and quantum phase diagram of spin- $\frac{1}{2}$ J_1 - J_2 - J_χ model on the square latticeXiao-Tian Zhang ¹, Yixuan Huang ^{2,3}, Han-Qing Wu,^{4,*} D. N. Sheng ^{5,†} and Shou-Shu Gong ^{6,7,‡}¹*School of Physics, Beihang University, Beijing 100191, China*²*Theoretical Division, Los Alamos National Laboratory, Los Alamos, New Mexico 87545, USA*³*Center for Integrated Nanotechnologies, Los Alamos National Laboratory, Los Alamos, New Mexico 87545, USA*⁴*Guangdong Provincial Key Laboratory of Magnetolectric Physics and Devices, School of Physics, Sun Yat-sen University, Guangzhou 510275, China*⁵*Department of Physics and Astronomy, California State University Northridge, Northridge, California 91330, USA*⁶*School of Physical Sciences, Great Bay University, Dongguan 523000, China*⁷*Great Bay Institute for Advanced Study, Dongguan 523000, China*

(Received 21 January 2024; accepted 11 March 2024; published 26 March 2024)

We study the spin-1/2 Heisenberg model on the square lattice with the first- and second-nearest-neighbor antiferromagnetic couplings J_1 and J_2 , as well as the three-spin scalar chiral coupling J_χ . Using density matrix renormalization group calculations, we obtain a quantum phase diagram of this system for $0 \leq J_2/J_1 \leq 1.0$ and $0 \leq J_\chi/J_1 \leq 1.5$. We identify the Néel and stripe magnetic order phase at small- J_χ coupling. With growing J_χ , we identify the emergent chiral spin liquid (CSL) phase characterized by the quantized spin Chern number $C = 1/2$ and entanglement spectrum with the quasidegenerate group of levels agreeing with chiral $SU(2)_1$ conformal field theory, which is an analog of the $\nu = 1/2$ Laughlin state in the spin system. In the vicinity of the Néel and CSL phase boundary, our numerical results do not find evidence to support the coexistence of Néel order and topological order that was conjectured by mean-field calculations. In the larger- J_2 and $-J_\chi$ coupling regime, the entanglement spectrum of the ground state also exhibits the chiral quasidegeneracy consistent with a CSL, but the adiabatic flux insertion simulations fail to obtain the quantized Chern number. By analyzing the finite-size scaling of the magnetic order parameter, we find the vanished magnetic order suggesting a magnetic disorder phase, whose nature needs further studies. Different from the spin-1 J_1 - J_2 - J_χ model, we do not find the coexistent stripe magnetic order and topological order. We also investigate the J_χ dominant regime and find a strong tendency of the system to develop a dimer order rather than the chiral spin magnetic order observed in the spin-1 model. Our results unveil interesting quantum phases in this spin-1/2 model and also demonstrate the drastic differences between the spin-1/2 and spin-1 cases.

DOI: [10.1103/PhysRevB.109.125146](https://doi.org/10.1103/PhysRevB.109.125146)**I. INTRODUCTION**

Quantum spin liquids (QSLs) are exotic states of matter in frustrated quantum magnets [1–5], which can escape from forming conventional orders even at zero temperature. Remarkably, QSLs have long-range quantum entanglement as well as fractionalized excitations [6–10]. Among the various types of QSLs, the chiral spin liquid (CSL) is a specific class of QSL that is an analog of the fractional quantum Hall state [11–15]. CSLs break time-reversal and parity symmetries but preserve lattice translational and spin rotational symmetries. Kalmeyer and Laughlin first proposed that, in a time-reversal-invariant spin model with geometric frustration, one may realize a CSL as the analog of the $\nu = 1/2$ Laughlin state through spontaneous time-reversal-symmetry breaking [11]. Later, based on the wave functions of fractional quantum Hall states, the parent Hamiltonians for which the CSLs are the

exact ground states have also been constructed in spin models with long-range interactions [16–18].

More interestingly, doping a CSL may lead to exotic anyon superconductivity [12, 19]. After extensive search for decades, this Kalmeyer-Laughlin CSL has been identified not only in various spin-1/2 systems with either geometric frustration or competing interactions [20–31], but also in the Hubbard model near the Mott transition [32–36]. Very recently, unbiased density matrix renormalization group (DMRG) studies have also established a $(d + id)$ -wave topological superconducting phase near the doped CSL regime [37–39].

On the other hand, CSL may also play an important role in cuprate superconductors. Recently, thermal Hall measurements for cuprate superconductors have found a giant thermal Hall conductivity at small doping level even including the half-filled case [40–44], which triggered the theoretical interests in the origin of thermal Hall conductivity [45–58]. Based on mean-field calculations, it was proposed that there is a coexistent regime of Néel magnetic order and CSL topological order [45, 50] in the spin-1/2 square-lattice Heisenberg model with the nearest-neighbor (NN) J_1 and next-nearest-neighbor (NNN) J_2 antiferromagnetic (AFM) exchange interactions, as

* wuhanq3@mail.sysu.edu.cn

† donna.sheng1@csun.edu

‡ shoushu.gong@gbu.edu.cn

well as the three-spin scalar chiral coupling J_χ describing the effect of external magnetic fields in the thermal Hall experiments. The coexistent Néel AFM order and neutral spinon excitations may provide a natural understanding of the experimental observations [45,50].

In previous studies on this microscopic spin model, the Néel AFM order and Kalmeyer-Laughlin CSL state have been found [28,51,59], but the possible coexistence has not been examined in numerical calculations. Very recently, the similar spin-1 J_1 - J_2 - J_χ model has been comprehensively studied by DMRG calculations, which find no evidence for coexistent Néel order and Abelian topological order but unveil a coexistence of stripe AFM order and a non-Abelian topological order in the larger- J_2 regime [60]. This coexistence is characterized by a strong magnetic order and the entanglement spectrum that agrees with the expected CSL state [60]. These reported results of the spin-1 model also stimulate an interest in the similar phenomenon in the corresponding spin-1/2 system.

In this work, we examine the quantum phase diagram of the spin-1/2 J_1 - J_2 - J_χ model on the square lattice (see the schematic figure on the left top corner of Fig. 1) by means of DMRG calculations, with the focus on exploring the possible coexistence of CSL topological order and magnetic order. In the studied parameter regime $0 \leq J_2/J_1 \leq 1.0$ and $0 \leq J_\chi/J_1 \leq 1.5$, we identify a Néel AFM phase, a stripe AFM phase, a CSL phase, and a magnetic disorder regime, as shown in Fig. 1. We confirm the CSL state by showing the quantized topological entanglement entropy $\gamma \simeq (\ln 2)/2$, chiral entanglement spectrum counting $\{1, 1, 2, 3, 5, \dots\}$, and quantized spin Chern number $C = 1/2$. Furthermore, we carefully investigate the phase transition from the Néel AFM phase to the CSL with growing chiral coupling. While the transition can be identified by various quantities, we do not find evidence to support a coexistence of topological order and Néel order near the phase boundary.

On the other hand, at the larger- J_2 side we find either the CSL state or a magnetic disorder state with increased J_χ coupling. While the entanglement spectrum of the ground state in the magnetic disorder regime can exhibit the quasidegenerate group of levels agreeing with chiral $SU(2)_1$ conformal field theory, the adiabatic flux insertion simulations fail to obtain a half-quantized spin Chern number in the studied system size. Meanwhile, the finite-size extrapolation of magnetic order parameters strongly suggests the absent magnetic order in this regime. Therefore, our DMRG results indicate that the coexistence of topological order and stripe AFM order observed in the spin-1 model [60] may not exist in the studied spin-1/2 case. In addition, we examine the J_χ -dominant regime where a chiral spin state (CSS) magnetic order [61] (see Appendix A) has been found in the spin-1 J_1 - J_2 - J_χ model [60]. Nonetheless, we do not find the CSS magnetic order but a strong tendency of the system to develop a dimer order spontaneously breaking lattice translational symmetry.

Compared with the spin-1 model, our results unveil the big differences between the spin-1/2 and spin-1 J_1 - J_2 - J_χ models, showing the important role of quantum fluctuations in the emergence of the different quantum states. In particular, the existence and absence of phase coexistence in the spin-1 and spin-1/2 systems may shed light on further investigation of

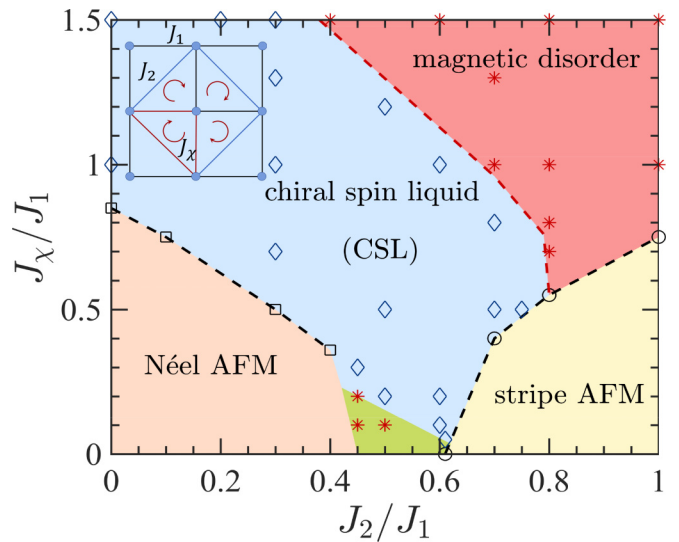


FIG. 1. Model illustration and phase diagram. The inset on the left top corner is a schematic illustration of the spin-1/2 J_1 - J_2 - J_χ Heisenberg model on the square lattice. J_1 and J_2 are the NN and NNN AFM interactions, respectively. J_χ is the magnitude of the three-spin chiral couplings $\mathbf{S}_i \cdot (\mathbf{S}_j \times \mathbf{S}_k)$ in the Hamiltonian in Eq. (1), which includes all the four kinds of triangles in each plaquette. For each triangle, the sites i , j , and k follow the same clockwise direction. The quantum phase diagram of the spin-1/2 J_1 - J_2 - J_χ model is obtained with $0 \leq J_2/J_1 \leq 1.0$ and $0 \leq J_\chi/J_1 \leq 1.5$. With tuning couplings, we identify the Néel AFM, stripe AFM, chiral spin liquid, and a magnetic disorder regime. The blue diamonds indicate the parameter points in which we can obtain a quantized spin Chern number $C = 1/2$ by the adiabatic flux insertion simulations on the $L_y = 8$ systems. For the intermediate J_2/J_1 regime with small- J_χ couplings, the red asterisks represent the parameter points where our DMRG simulations do not obtain a quantized Chern number. In the magnetic disorder regime, the entanglement spectrum of the ground state shows the chiral counting consistent with a chiral spin liquid, but the flux insertion simulations fail to obtain a quantized Chern number.

the coexisting topological order and conventional order. We also discuss the potential nature of the magnetic disorder regime, which we leave for future study.

The organization of our paper is as follows: In Sec. II, we introduce the model and the details of DMRG calculations. In Sec. III, we identify the phase diagram at the smaller J_2 side. We characterize the CSL state and show the phase transition from the Néel to the CSL phase. We also explore the possible phase coexistence between the two phases. In Sec. IV, we discuss the quantum phases at the larger- J_2 side and carefully examine the properties of the magnetic disorder regime. In Sec. V, we go beyond the phase diagram in Fig. 1 and discuss the possible dimer order phase in the J_χ -dominant regime. We summarize the results in Sec. VI.

II. MODEL HAMILTONIAN AND METHODS

We consider the spin-1/2 square-lattice model with the NN (J_1) and NNN (J_2) AFM Heisenberg interactions, as well as the three-spin scalar chiral coupling J_χ for all four small triangles in each plaquette of the square lattice. The Hamiltonian

is defined as

$$H = \sum_{\langle i, j \rangle} J_1 \mathbf{S}_i \cdot \mathbf{S}_j + \sum_{\langle\langle i, j \rangle\rangle} J_2 \mathbf{S}_i \cdot \mathbf{S}_j + \sum_{\Delta} J_{\chi} \mathbf{S}_i \cdot (\mathbf{S}_j \times \mathbf{S}_k), \quad (1)$$

where the sums $\langle i, j \rangle$ and $\langle\langle i, j \rangle\rangle$ run over all the NN and NNN bonds, respectively. The chiral couplings involve the sum over all four kinds of triangles in each plaquette, where the sites i, j , and k follow the same clockwise direction as shown in Fig. 1.

We determine the quantum phases of the model by using DMRG [62] calculations. In DMRG simulation, we study the system on the cylinder geometry with the periodic boundary conditions along the circumference direction (y direction) and the open boundary conditions along the axis direction (x direction). We denote L_y and L_x as the site numbers in the two directions, respectively. We implement the spin SU(2) symmetry [63] in the finite DMRG simulations, which allows us to study the systems with circumference up to $L_y = 12$. We keep the bond dimensions up to 6000 SU(2) multiplets, which are equivalent to about 24000 U(1) states. For the $L_y = 12$ systems, the DMRG truncation error is smaller than 5×10^{-5} , while for smaller L_y systems, we can obtain very accurate results with the truncation error smaller than 1×10^{-6} . In addition, we use the TeNPy [64] package to perform the infinite DMRG simulations on systems with the circumference up to $L_y = 8$, in which we keep the bond dimensions up to 3000 U(1) states, with the truncation error near 10^{-5} .

We obtain the quantum phase diagram of the model at $0 \leq J_2/J_1 \leq 1.0$ and $0 \leq J_{\chi}/J_1 \leq 1.5$, as shown in Fig. 1. We set $J_1 = 1.0$ as the energy unit. In the presence of a moderate chiral coupling, we identify two magnetic order phases, a CSL phase, and a magnetic disorder regime in the studied parameter region. For the intermediate nonmagnetic regime $J_2/J_1 \sim 0.55$, we find that the CSL state can be easily driven by a small chiral coupling.

III. NÉEL ORDER, CHIRAL SPIN LIQUID, AND THE PHASE TRANSITION

In this section, we will demonstrate our numerical results to identify the Néel AFM phase, CSL phase, and the phase transition. We will also discuss our investigation of the possible phase coexistence.

A. Néel phase and the phase transition

For $J_2 = J_{\chi} = 0$, the system possesses a Néel AFM order, which would be suppressed by the increased J_{χ} coupling. With growing chiral coupling, a transition from the Néel order to the CSL has been proposed at $J_{\chi}/J_1 \simeq 0.189$ by exact diagonalization calculation [28], showing that the AFM order will be easily melted by chiral coupling. On the other hand, a recent exact diagonalization calculation of quantum fidelity on a 4×4 cluster suggests the transition at $J_{\chi}/J_1 \simeq 0.7$ [51], and a spinon mean-field study finds the transition at $J_{\chi}/J_1 \simeq 1.35$ [59].

To accurately determine the phase transition with vanishing Néel order, we first compute the Néel order parameter

$m^2(\pi, \pi)$ defined as

$$m^2(\vec{k}) = \frac{1}{N_m^2} \sum_{i, j} \langle \mathbf{S}_i \cdot \mathbf{S}_j \rangle e^{i\vec{k} \cdot (\vec{r}_i - \vec{r}_j)} \quad (2)$$

at the momentum $\vec{k} = (\pi, \pi)$. In the summation of the above equation, we only consider the middle $N_m = L_y \times L_y$ sites on a long cylinder to avoid the edge effects. In Fig. 2(a), we show $m^2(\pi, \pi)$ with growing J_{χ}/J_1 for $L_y = 4, 6, 8$ ($J_2 = 0$), which all have a behavior change at $J_{\chi}/J_1 \simeq 0.85$ that can be clearly identified in the derivative as shown in the inset of Fig. 2(a). In Fig. 2(b), we further analyze the finite-size scaling of $m^2(\pi, \pi)$ with $L_y = 4, 6, 8, 10$, which is extrapolated using polynomial fitting up to the second order of $1/L_y$. The extrapolated results support a transition with vanished Néel AFM order at $J_{\chi}/J_1 \simeq 0.85$, which is consistent with the finding in Fig. 2(a).

Since the phase transition may be characterized by the ground-state energy, we also study the scalar chiral order parameter $\langle \chi \rangle$ in the bulk of the cylinder versus J_{χ}/J_1 . The chiral order is defined as $\langle \chi \rangle \equiv \langle \mathbf{S}_i \cdot (\mathbf{S}_j \times \mathbf{S}_k) \rangle$, where the sites i, j , and k follow the definition of the small triangle shown in the inset of Fig. 1. Thus, this chiral order is equivalent to the first-order derivative of the ground-state energy with respect to the chiral coupling. The obtained chiral orders on different system sizes [Fig. 2(c)] and their derivatives shown in the inset also characterize a transition at $J_{\chi}/J_1 \simeq 0.85$. Therefore, our DMRG results indicate that a chiral coupling as large as the Heisenberg interaction J_1 is required to suppress the Néel order. In the same way, we can determine the phase boundary with vanishing the Néel order in Fig. 1. More data can be found in Fig. 12 (see Appendix B).

B. Identification of the chiral spin liquid

With suppressed Néel order by increasing the chiral coupling, we can identify an emergent gapped Kalmeyer-Laughlin CSL by DMRG calculations, which is equivalent to the $\nu = 1/2$ bosonic fractional quantum Hall state [11]. First of all, we calculate the spin-triplet gap. We obtain the gap in the bulk by calculating the lowest-energy states in the total spin $S = 0$ and $S = 1$ sectors for the middle $L_y \times L_y$ sites by DMRG. We first calculate the ground state in the $S = 0$ sector on a long cylinder and then sweep the $S = 1$ sector for the middle $L_y \times L_y$ sites, which can avoid the edge excitations [65]. In Fig. 3(a), we show the system size dependence of the triplet gap obtained on the $L_y = 4, 6, 8$ systems at different J_{χ} and $J_2 = 0$. One can see that the gaps drop fast versus $1/L_y$ and go to zero in the thermodynamic limit at $J_{\chi}/J_1 = 0.8$, consistent with the Néel AFM order with gapless Goldstone modes. In contrast, for $J_{\chi}/J_1 = 1.0$ and 1.2 , the gaps are extrapolated to finite values, showing the gapped spin-triplet excitations.

Next, we identify the quantized topological entanglement entropy of the Kalmeyer-Laughlin CSL by analyzing the circumference dependence of entanglement entropy [66]. For gapped topological states, the entanglement entropy follows the area law and thus mainly depends on the system circumference L_y [67]. In particular, the entropy $S(L_y)$ of the minimum entangled state with a smooth boundary of length L_y will take

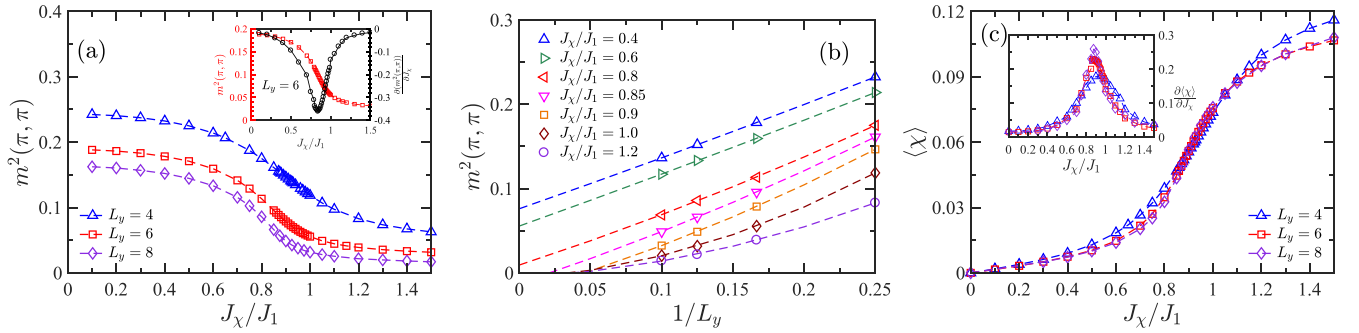


FIG. 2. Quantum phase transition with vanishing Néel AFM order by chiral coupling at $J_2 = 0$. (a) Néel AFM order parameter $m^2(\pi, \pi)$ versus J_x/J_1 . The data of $m^2(\pi, \pi)$ are obtained from the middle $L_y \times L_y$ sites of a long cylinder system with $L_y = 4, 6, 8$. The inset is the J_x/J_1 dependence of $m^2(\pi, \pi)$ and its first-order derivative for $L_y = 6$. (b) Finite-size scaling of $m^2(\pi, \pi)$ with $L_y = 4, 6, 8, 10$ for different J_x/J_1 . The dashed lines denote the polynomial fittings up to the second order of $1/L_y$. (c) Scalar chiral order $\langle \chi \rangle$ versus J_x/J_1 on different system sizes. The chiral order defined as $\langle \chi \rangle \equiv \langle \mathbf{S}_i \cdot (\mathbf{S}_j \times \mathbf{S}_k) \rangle$ is measured in the bulk of the long cylinder and is uniform. The four kinds of triangles in each plaquette have the same magnitude of chiral order. The inset shows the first-order derivative of the chiral order with respect to J_x/J_1 , which is equivalent to the second-order derivative of ground-state energy. The symbols in (c) and its inset follow the same definitions.

the form

$$S(L_y) \simeq aL_y - \gamma, \quad (3)$$

where γ is the topological entanglement entropy, which is a universal additive constant characterizing the long-range entanglement in the ground state and is related to the total quantum dimension D of a topological order as $\gamma = \ln D$ [68,69]. The coefficient a is nonuniversal due to the short-distance physics near the boundary. In DMRG calculation, it is straightforward to obtain the entanglement entropy by bipartitioning the whole system into two subsystems. The entropy can be obtained as $S = -\sum_i \lambda_i \ln \lambda_i$, where λ_i are the eigenvalues of the reduced density matrix of the subsystems. In the inset of Fig. 3(b), the entropy versus subsystem length shows that the entropy is almost independent of the subsystem length, which agrees with the area law of entanglement entropy for such a quasi-one-dimensional gapped system [67]. Since DMRG simulation on topological order states would

naturally find the minimum entangled state [66], in Fig. 3(b), we can study the scaling of the obtained entropy $S(L_y)$ versus L_y ($L_y = 6, 8, 10$) for $J_x/J_1 = 1.0$ and 1.2 . Notice that the entropy data for each L_y are obtained on long cylinders, which is almost independent of cylinder length and can be taken as the result in the $L_x \rightarrow \infty$ limit. Following Eq. (3), we fit our entropy data linearly with the red asterisk showing the theoretical prediction $\gamma = (\ln 2)/2$ for the Kalmeyer-Laughlin CSL [69]. One can see that although the finite-size effects may exist, the extrapolated γ at $J_x/J_1 = 1.0, 1.2$ are very close to $(\ln 2)/2$, which highly agrees with the Kalmeyer-Laughlin CSL state.

Furthermore, we calculate the entanglement spectrum to characterize the CSL state because the entanglement spectrum has a one-to-one correspondence with the physical edge spectrum [70,71]. We use the quantum number total S^z of the half system and the relative momentum quantum number along the y direction, Δk_y to label the obtained eigenvalues of the

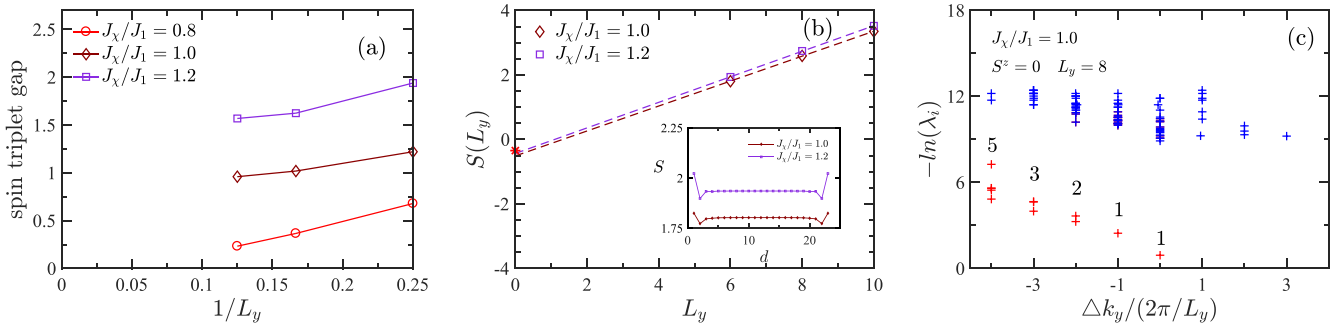


FIG. 3. Identification of the chiral spin liquid state at $J_2 = 0$. (a) Finite-size scaling of the spin-triplet gap, which is obtained for the middle $L_y \times L_y$ sites on the $L_y = 4, 6, 8$ systems. We show the results in both Néel AFM phase ($J_x/J_1 = 0.8$) and chiral spin liquid phase ($J_x/J_1 = 1.0, 1.2$), which are clearly extrapolated to vanished and finite, respectively. (b) Entanglement entropy S versus cylinder circumference L_y , at $J_x/J_1 = 1.0, 1.2$. We fit the data by the formula $S = aL_y - \gamma$. The red asterisk shows the theoretical prediction $\gamma = (\ln 2)/2$ for the $\nu = 1/2$ Laughlin state. The inset shows the entanglement entropy obtained for different subsystem length d , which follows the area law of entropy. (c) Entanglement spectrum labeled by the quantum numbers of total spin $S^z = 0$ and relative momentum along the y direction Δk_y . λ_i is the eigenvalue of reduced density matrix. We show the results for $J_x/J_1 = 1.0$ at the $L_y = 8$ system. The numbers $\{1, 1, 2, 3, 5\}$ denote the near-degenerate low-lying levels separated by an entanglement gap from higher levels, which agrees with the prediction of the $SU(2)_1$ conformal field theory. In the figure, the smaller eigenvalues are not shown.

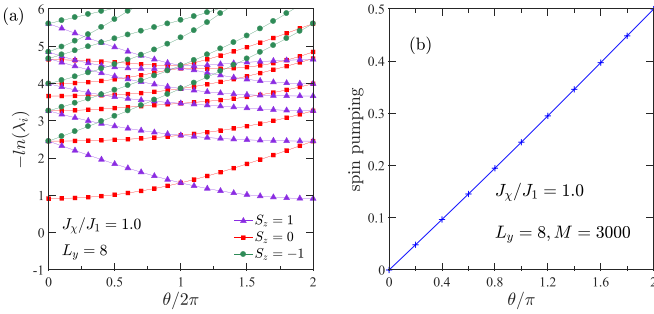


FIG. 4. Adiabatic flux insertion simulation and quantized spin Chern number for $J_x/J_1 = 1.0$, $J_2 = 0$ on the $L_y = 8$ cylinder. (a) Entanglement spectrum flow with adiabatically inserted flux θ , which is obtained by iDMRG simulation with 1000 bond dimensions. The eigenvalues in the $S_z = 0, \pm 1$ sectors are labeled by different symbols. (b) Spin pumping with adiabatically inserted flux θ , which is obtained by iDMRG simulation with 3000 bond dimensions. In a period of inserted flux $\theta = 0 \rightarrow 2\pi$, a quantized magnetization moment 0.5 is accumulated at one open boundary of the cylinder, indicating a fractionally quantized spin Chern number $C = 1/2$.

reduced density matrix [72,73]. In Fig. 3(c), we present the entanglement spectrum of the ground state at $J_x/J_1 = 1.0$ on the $L_y = 8$ cylinder, which is obtained for the total $S^z = 0$ sector. The spectrum clearly shows the quasidegenerate pattern $\{1, 1, 2, 3, 5, \dots\}$ with increasing Δk_y , and the quasidegenerate levels are well separated from the higher levels by an entanglement gap. Such a chiral structure of entanglement spectrum agrees with the $SU(2)_1$ conformal field theory prediction and supports a Kalmeyer-Laughlin CSL [74].

At last, we compute the spin Chern number through adiabatic flux insertion and the change of entanglement spectrum with increased flux [15,21]. Since inserting a flux along the cylinder is equivalent to imposing the twist boundary conditions in the circumference (y) direction, we consider the flux by replacing the spin-flipping term $S_i^+ S_j^- + \text{H.c.}$ to $S_i^+ S_j^- e^{i\theta} + \text{H.c.}$ for these Heisenberg interacting bonds crossing the y boundary. For the chiral interactions crossing the y boundary, we introduce the similar changes in the Hamiltonian terms. We take one component $S_i^+ S_j^- S_k^z + \text{H.c.}$ as an example, which is replaced as $S_i^+ S_j^- S_k^z e^{i\theta} + \text{H.c.}$ in the presence of flux. We adiabatically increase the flux by taking the obtained ground state at a given flux θ as the initial state for the next-step simulation of the added flux $\theta + \Delta\theta$. The entanglement spectrum versus the adiabatically added flux is shown in Fig. 4(a) for $J_2 = 0$, $J_x/J_1 = 1.0$, where the eigenvalues $-\ln \lambda_i$ in the $S^z = -1, 0, 1$ sectors are demonstrated. By analyzing the distributions of the eigenvalues at each given flux, one can find that while the spectrum is symmetric about $S^z = 0$ at zero flux, $\theta = 0$, it becomes symmetric about $S^z = 1/2$ at $\theta = 2\pi$ flux, which agrees with a spin-1/2 spinon at each end of the cylinder for the system with $\theta = 2\pi$. Correspondingly, the system evolves from the vacuum sector ($\theta = 0$) to the spinon sector ($\theta = 2\pi$). With further increase of the flux from 2π to 4π , the entanglement spectrum becomes symmetric about $S^z = 1$, indicating that the system evolves back to the vacuum sector at $\theta = 4\pi$.

By means of this adiabatic flux insertion, we can also compute the spin Chern number. In fractional quantum Hall states, a quantized net charge transfer would appear as $\Delta N = C$ from one edge of the sample to the other edge after inserting a period of flux $\theta = 0 \rightarrow 2\pi$, corresponding to a fractionally quantized topological invariant Chern number C [75]. Following this method, we can measure the local spin magnetization moment $\langle S_{i,j}^z \rangle$ for each site (i, j) at each flux [21]. In the process of inserting flux, one can find that the magnetizations in the bulk remain unchanged but only change near the open boundaries, which is equivalent to spin transfer from one edge to the other one. In a period of flux insertion, the transferred total spin gives the spin Chern number. As shown in Fig. 4(b) for $J_2 = 0$ and $J_x/J_1 = 1.0$, the fractionally quantized spin transfer 0.5 characterizes the spin Chern number $C = 1/2$, which agrees with a Kalmeyer-Laughlin CSL state. An additional example at $J_2 > 0$ is demonstrated in Fig. 13 (see Appendix C).

C. Investigation on the possible phase coexistence

Between the Néel AFM and CSL phase, a possible coexistence regime has been proposed based on the mean-field theory [45], which is expected to exhibit both the Néel AFM order and topological order. In a recent DMRG study of the spin-1 square-lattice J_1 - J_2 - J_x model, a coexistence of stripe AFM order and non-Abelian topological order is suggested, which is characterized by the finite magnetic order and chiral entanglement spectrum [60]. Such a combination of numerical results could be taken as the primary evidence of this kind of coexistence of magnetic order and topological order. In our study, we follow the same strategy to investigate the possible phase coexistence.

We focus on the small parameter regime below the Néel order boundary in Fig. 1, in which the system still possesses the Néel AFM order. Here, we investigate the possible topological order by studying the entanglement spectrum and Chern number. By DMRG simulations, we find that even if we choose the parameter point very close to the boundary such as $J_2 = 0$, $J_x/J_1 = 0.8$, either the quasidegenerate chiral pattern of the entanglement spectrum or the quantized Chern number is not obtained, as shown in Fig. 5. The entanglement spectrum we obtain should be interpreted as evolving towards that of the CSL with increased chiral coupling. On the other hand, above the boundary when the Néel AFM order vanishes, both the entanglement spectrum and Chern number simulation results are consistent with an emergent CSL state. Near this phase boundary at finite J_2 , our DMRG results lead to the same conclusion. Therefore, our results do not support the coexistence of Néel order and CSL that was conjectured by mean-field calculations [45].

IV. STRIPE PHASE AND THE MAGNETIC DISORDER REGIME

For the intermediate $J_2/J_1 \sim 0.55$ regime in the J_1 - J_2 model, we find that a small- J_x coupling can lead to the emergent CSL state with the characteristic Chern number $C = 1/2$, as shown in Fig. 14 of Appendix C. For the stripe AFM phase at larger J_2/J_1 , our DMRG results identify either a

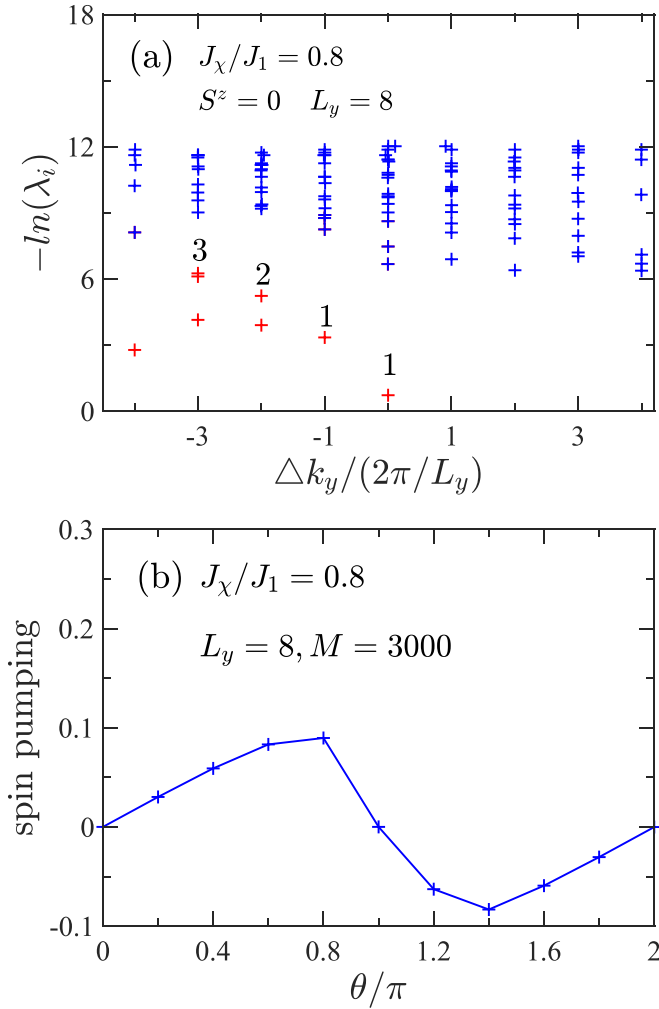


FIG. 5. Exploring the possible coexistence of magnetic order and topological order. (a) Entanglement spectrum labeled by the quantum numbers of total spin $S^z = 0$ and relative momentum along the y direction, Δk_y . λ_i is the eigenvalue of reduced density matrix. (b) Spin pumping with adiabatically inserted flux θ . We consider the parameter at $J_2/J_1 = 0$, $J_x/J_1 = 0.8$ on the $L_y = 8$ cylinder.

CSL state or a magnetic disorder state while the stripe order is suppressed by the increased J_x coupling. In this magnetic disorder state, the entanglement spectrum of the ground state shows the quasidegenerate pattern $\{1, 1, 2, 3, \dots\}$, but the flux insertion simulations fail to obtain a quantized spin Chern number. Next, we will demonstrate the details of the DMRG results.

A. Stripe phase and the phase transition

For $J_x = 0$, the J_1 - J_2 model exhibits a stripe AFM order for $J_2/J_1 \gtrsim 0.61$ [76]. With increased chiral coupling, the stripe order will be suppressed. To identify the phase transition with vanishing stripe order, we investigate the spin structure factor and chiral order parameter.

For the stripe AFM order on the square lattice, the spin structure factor on a finite symmetric lattice should have peaks at both $\vec{k} = (0, \pi)$ and $(\pi, 0)$. In our DMRG calculations on long-cylinder geometry, the spin correlations form the stripe

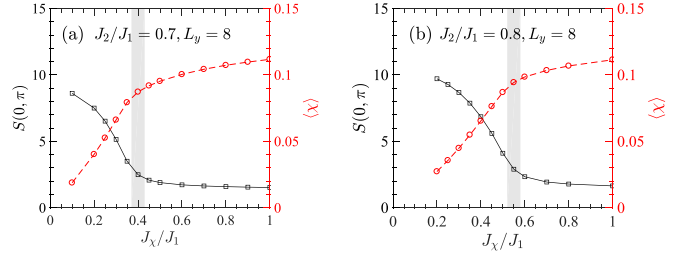


FIG. 6. Quantum phase transition with vanishing stripe AFM order by tuning chiral coupling. The spin structure factor $S(0, \pi)$ which characterizes the stripe order and the scalar chiral order parameter $\langle \chi \rangle$ are shown versus J_x/J_1 on the $L_y = 8$ systems for (a) $J_2 = 0.7$ and (b) $J_2 = 0.8$. The shades denote the phase transitions.

pattern along a certain direction because of the geometry, and the spin structure factor selects the peak at $\vec{k} = (0, \pi)$. Therefore, we study $S(0, \pi)$ versus the tuning chiral coupling. In Fig. 6, we show the structure factor $S(0, \pi)$ and chiral order parameter $\langle \chi \rangle$ for $J_2/J_1 = 0.7$ and 0.8 on the $L_y = 8$ cylinder. As marked by the shades, both quantities consistently characterize a phase transition with the vanished stripe AFM order. One can find that while the J_x dependence of chiral order exhibits a clear change characterizing a continuous-like phase transition (the red curve), the stripe AFM structure factor $S(0, \pi)$ drops fast to quite small values (the black curve), which is consistent with the transition described by the change of chiral order $\langle \chi \rangle$.

In the spin-1 J_1 - J_2 - J_x model, the DMRG calculations find evidence for the coexistence of stripe order and non-Abelian topological order [60]. Therefore, in the stripe AFM phase of the studied spin-1/2 model, we also examine the entanglement spectrum and Chern number, but our results do not support a coexistent topological order in the stripe phase (not shown here).

B. The magnetic disorder regime

Next, we focus on the discussion of the magnetic disorder regime based on the DMRG results. In this magnetic disorder regime, the entanglement spectrum of the obtained ground state also exhibits the quasidegenerate chiral counting $\{1, 1, 2, 3, 5, \dots\}$ and a large entanglement gap that separates the quasidegenerate levels from the higher levels, as shown in Fig. 7 of the $L_y = 8$ systems. The entanglement spectrum results may indicate the obtained ground state as the vacuum sector of a CSL state. Nonetheless, the spin accumulation in the adiabatic flux insertion simulation is found to collapse at a flux θ smaller than 2π , as demonstrated in the insets of Fig. 7. Consequently, the ground state at $\theta = 2\pi$ is the same as that at $\theta = 0$, namely, the flux insertion simulations fail to find the spin topological sector as expected for a CSL.

Furthermore, we explore possible magnetic order in this regime and provide DMRG data to support the absent magnetic order. First of all, we carefully examine the spin structure factor in the region of $0.6 \leq J_2/J_1 \leq 1.0$ and $0 \leq J_x/J_1 \leq 1.5$ on the $L_y = 8$ cylinder. We find that when the stripe AFM order is suppressed as we identify in Fig. 6, the spin structure factor shows small peaks at $\vec{k} = (0, \pi)$, $(\pi, 0)$, and

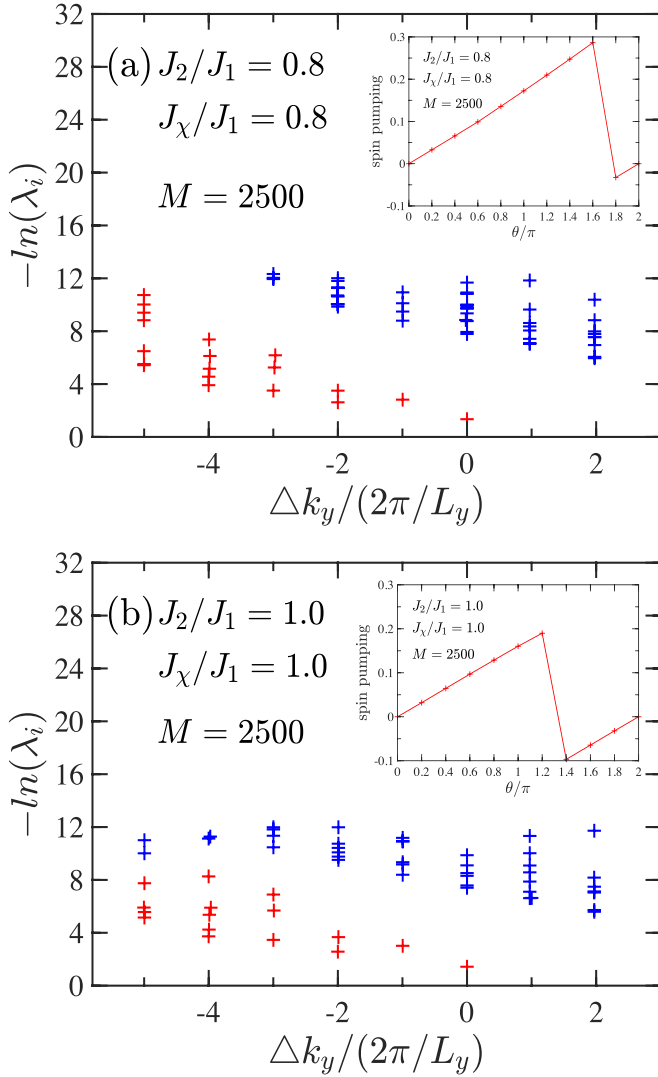


FIG. 7. Entanglement spectrum and adiabatic flux insertion simulations in the magnetic disorder regime. [(a) and (b)] The entanglement spectrum labeled by the quantum numbers of total spin $S^z = 0$ and relative momentum along the y direction, Δk_y , for the ground states of $J_2/J_1 = J_\chi/J_1 = 0.8$ and $J_2/J_1 = J_\chi/J_1 = 1.0$, respectively, on the $L_y = 8$ cylinder systems. λ_i are the eigenvalues of reduced density matrix. The results are obtained by keeping 2500 U(1) states. The insets show the spin pumping with adiabatically inserted flux θ . At a flux smaller than 2π , the spin accumulation collapses. As a result, the obtained ground state at $\theta = 2\pi$ is the same as that at zero flux.

$(\pi/2, \pi/2)$ in the magnetic disorder regime (see Fig. 15 in Appendix D), which implies a possible weak CSS magnetic order [61]. To detect such a possible magnetic order, we calculate the corresponding magnetic order parameters $m^2(0, \pi)$, $m^2(\pi, 0)$, and $m^2(\pi/2, \pi/2)$ and make the finite-size extrapolations to estimate the results in the thermodynamic limit. Notice that we only consider the results on the $L_y = 4, 8, 12$ systems, which are compatible with the structure factor peak at $\vec{k} = (\pi/2, \pi/2)$.

We first examine the coupling dependence of the spin structure factor at $\vec{k} = (0, \pi)$, $(\pi, 0)$, and $(\pi/2, \pi/2)$ on the

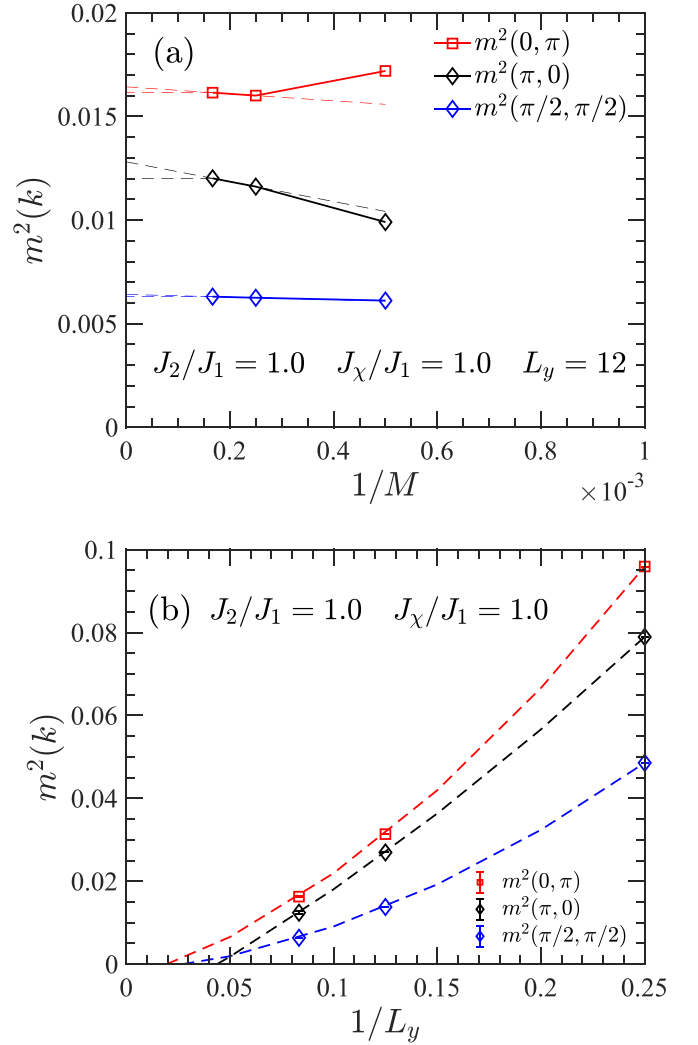


FIG. 8. Analyses of magnetic order parameters at $J_2/J_1 = J_\chi/J_1 = 1.0$. (a) Bond dimension dependence of the magnetic order parameters $m^2(0, \pi)$, $m^2(\pi, 0)$, and $m^2(\pi/2, \pi/2)$ with bond dimensions $M = 2000, 4000$, and 6000 on the $L_y = 12$ cylinder. We estimate the error bar of the extrapolation by using the $M = 6000$ result and the linearly extrapolated result by using $M = 4000$ and 6000 data (the dashed line). (b) Finite-size scaling of the magnetic order parameters $m^2(0, \pi)$, $m^2(\pi, 0)$, and $m^2(\pi/2, \pi/2)$ with $L_y = 4, 8, 12$. The error bars of the $L_y = 12$ data determined from (a) are also shown, which are very small.

$L_y = 8$ system (see Fig. 15 in Appendix D), which shows the parameter points with the strongest structure factors on this finite-size system. Furthermore, we make the finite-size scaling of these magnetic order parameters at the parameter points with strong spin structure factor. Due to the computation cost of the complex wave function, we keep the bond dimensions up to 6000 SU(2) multiplets, which can give well-converged results for $L_y = 4$ and 8 , but less converged results for $L_y = 12$. Therefore, we analyze the bond dimension dependence of the magnetic order parameters for $L_y = 12$ to estimate the results in the infinite-bond-dimension limit, as shown in Fig. 8(a) for $J_2/J_1 = J_\chi/J_1 = 1.0$. We keep $M = 2000, 4000$, and 6000 SU(2) multiplets to obtain the magnetic

order parameters, and plot the results versus $1/M$. While $m^2(0, \pi)$ and $m^2(\pi/2, \pi/2)$ seem to approach convergence with bond dimension, the extrapolated $m^2(\pi, 0)$ may have the relatively larger error bar. We estimate the error bar of the extrapolation by using the $M = 6000$ result and the linearly extrapolated result by considering $M = 4000$ and 6000 , which are taken as the lower and upper boundaries of the $M \rightarrow \infty$ result. In Fig. 8(b), we make the finite-size scaling for the three order parameters with $L_y = 4, 8, 12$, which all decay fast with system width and are smoothly extrapolated to vanish. Notice that since the error bars of the $L_y = 12$ results are quite small, the uncertainties of the results do not change our conclusion. We have also checked the size-scaling results at $J_2/J_1 = 0.8$, $J_\chi/J_1 = 0.7$ and $J_2/J_1 = 0.8$, $J_\chi/J_1 = 1.0$ (see Fig. 16 in Appendix D), which all agree with no magnetic order. Therefore, our finite-size scaling analyses of the magnetic order parameters suggest no magnetic ordering in this regime, which could be consistent with the ground state that appears like a CSL state in the vacuum topological sector, as characterized by the entanglement spectrum in Fig. 7.

V. STRONG TENDENCY TO FORM A DIMER ORDER AT LARGE CHIRAL COUPLING

In this section, we extend our discussion to the large chiral coupling regime, which is beyond the parameter region of Fig. 1. Classically, the dominant chiral coupling J_χ in this system will lead to the magnetically ordered CSS [61]. In a recent DMRG study of the spin-1 J_1 - J_2 - J_χ model, the CSS has also been identified in the large- J_χ regime [60].

Here, we examine the spin-1/2 case. We first measure the spin structure factor to detect the possible CSS magnetic order. Since the spin pattern of the CSS order has the translational period of 4 along both the x and y directions (see Fig. 11 in Appendix A), we choose the system circumference $L_y = 4, 8$ to accommodate this spin pattern. Indeed, the spin structure factor $S(\mathbf{k})$ exhibits peaks at $\mathbf{k} = (\pi, 0)$, $(0, \pi)$ and $(\pm\frac{\pi}{2}, \pm\frac{\pi}{2})$, as shown in Fig. 9 of the pure J_χ model on the $L_y = 8$ system. The peak momenta fully agree with the feature of the CSS state [60]. Nonetheless, one can find in Fig. 9 that all the peaks of $S(\mathbf{k})$ are very broad, which indicates that the CSS magnetic order is likely to be melted by the stronger quantum fluctuations in the spin-1/2 case while this order can persist in the spin-1 case [60]. One possibility of this nonmagnetic state could be the CSL, which however is not supported by the DMRG results.

Therefore, we turn to explore a possible translational symmetry breaking for large- J_χ coupling. To accommodate the short-range spin configurations as shown in Fig. 9, we study the $L_y = 4, 8, 12$ cylinders. However, at large J_χ , the DMRG calculations are harder to converge, which makes the good convergence for $L_y = 12$ more difficult. Thus, we will mainly rely on the well-converged $L_y = 4, 8$ results and also refer to the less-converged results for $L_y = 12$.

We study the decay length of the boundary-induced dimer order and its circumference dependence, which has been found efficient to identify a bond dimer state even if the dimer order is very weak [77,78]. Here, we briefly introduce the strategy of this method. Since our DMRG calculations are performed on the cylinder geometry with open boundary

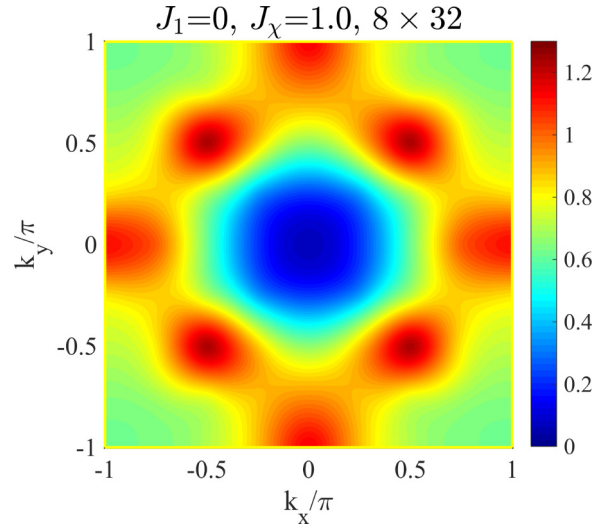


FIG. 9. Spin structure factor for $J_1 = 0$, $J_\chi = 1.0$. The structure factor is obtained from the Fourier transformation of spin correlations of the middle $L_y \times L_y$ sites on the $L_y = 8$, $L_x = 32$ cylinder, which shows round peaks at $\mathbf{k} = (\pi, 0)$, $(0, \pi)$, and $(\pm\frac{\pi}{2}, \pm\frac{\pi}{2})$. These peak momenta agree with that in the CSS magnetic order state, but the very broad peaks indicate the vanished magnetic order.

conditions, the translational symmetry along the x direction has already been broken, which leads to a dimer order of the bond energy $\langle \mathbf{S}_i \cdot \mathbf{S}_j \rangle$. We define the dimer order parameter D_x as the bond energy difference between the two neighboring horizontal bonds,

$$D_x(d) = \langle \mathbf{S}_{(d,y)} \cdot \mathbf{S}_{(d+1,y)} \rangle - \langle \mathbf{S}_{(d+1,y)} \cdot \mathbf{S}_{(d+2,y)} \rangle, \quad (4)$$

where $\mathbf{S}_{(d,y)}$ denotes the spin on the position (d, y) . Therefore, on finite-size systems, D_x would decay exponentially from the edge to the bulk as $D_x \sim e^{-d/\xi_x}$. If the ground state is a dimer order state in two dimensions, the decay length ξ_x would grow rapidly with increased system circumference and eventually diverge in a certain width when spontaneous symmetry breaking can happen. Otherwise, in a state without a dimer order, the decay length ξ_x would be a finite number in the thermodynamic limit.

Following this strategy, we compute the dimer order D_x on different systems. In Fig. 10, we show the log-linear plot of D_x for $J_\chi = 1.0$, $J_1 = 0$ on different sizes. On the smaller $L_y = 4, 8$ systems, D_x decays exponentially and ξ_x grows rapidly from $\xi_x \simeq 2.02$ to 5.09 . On the wider $L_y = 12$ system, we push the calculations up to 5000 SU(2) multiplets, and the results show a strong dimer order. Although the $L_y = 12$ results are less converged, the strong dimer order and the quickly growing ξ_x from $L_y = 4$ to $L_y = 8$ strongly suggest a dimer order in the two-dimensional limit. This tendency to develop a dimer order at large chiral coupling is also suggested by the growing ξ_x with increased J_χ coupling (see Fig. 17 in Appendix E). While the CSS is robust in the spin-1 system, the magnetic order seems to give way to a magnetically disordered dimer state in the spin-1/2 system due to the stronger quantum fluctuations.

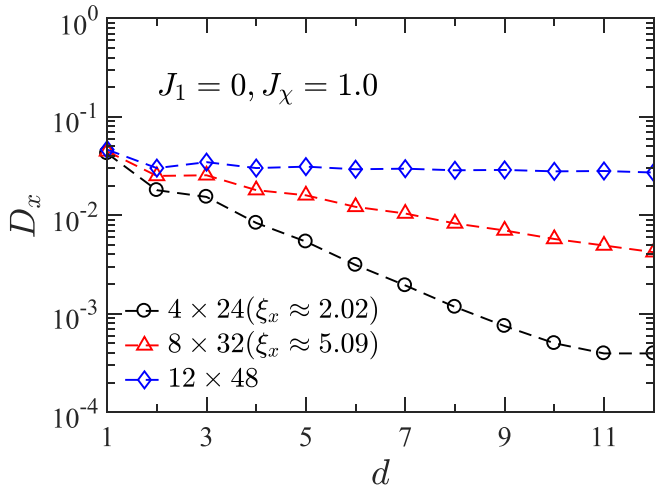


FIG. 10. Log-linear plot of the horizontal bond dimer order D_x versus the distance d away from the open boundary. The system is the pure J_χ model with $J_\chi = 1.0$, $J_1 = J_2 = 0$ on the $L_y = 4$, $L_x = 24$, $L_y = 8$, $L_x = 32$, and $L_y = 12$, $L_x = 48$ cylinders. The exponential fitting of $D_x \sim e^{-d/\xi_x}$ gives the decay length $\xi_x \approx 2.02$ and 5.09 for $L_y = 4$ and 8 cylinders, respectively. The $L_y = 12$ results are obtained with the bond dimensions $M = 5000$.

VI. SUMMARY AND DISCUSSION

We have studied the quantum phase diagram of the spin-1/2 J_1 - J_2 - J_χ model on the square lattice using DMRG calculations. This model was expected to give some insight for the giant thermal Hall conductivity in cuprate superconductors [45–51]. By mean-field calculation, a phase coexistence of Néel AFM order and topological CSL was proposed in this model, which could be used to explain the enhanced thermal Hall response in some cuprate materials [45,50]. On the other hand, a recent DMRG study of the spin-1 J_1 - J_2 - J_χ model identifies the coexistence of stripe AFM order and non-Abelian CSL topological order. The reported coexistence of magnetic order and topological order motivates us to examine the quantum phases and possible coexistence in this spin-1/2 model.

By tuning the interactions $0 \leq J_2/J_1 \leq 1.0$ and $0 \leq J_\chi/J_1 \leq 1.5$, we identify the Néel AFM phase, stripe AFM phase, CSL phase, and a magnetic disorder regime, as shown in Fig. 1. For the intermediate nonmagnetic region $J_2/J_1 \approx 0.5$ of the J_1 - J_2 model, we find that a small chiral coupling can drive the emergence of the CSL state. However, the related phase transition requires numerical studies of much larger length scales, which is beyond the scope of this work.

With growing chiral coupling, we identify the phase transition with vanishing Néel AFM order by examining the Néel order parameter $m^2(\pi, \pi)$ and scalar chiral order parameter $\langle \chi \rangle$. Above this phase boundary, we can verify the Kalmeyer-Laughlin CSL phase by the characteristic features including the quantized topological entanglement entropy $\gamma = (\ln 2)/2$, chiral entanglement spectrum agreeing with the $SU(2)_1$ conformal field theory, and spin Chern number $C = 1/2$. Below the phase boundary when the Néel order exists, we explore the possible phase coexistence. Nonetheless, either the entanglement spectrum or Chern number result does not support a coexistent topological order. Even near the phase

boundary with a very weak Néel order, the entanglement spectrum does not form the chiral structure of the CSL but exhibits an evolution towards the spectrum of a CSL, which suggests no coexistence of magnetic and topological order.

For the stripe phase at larger J_2/J_1 , we find two regimes when the stripe AFM order is suppressed by increased chiral coupling. One regime is identified as the same CSL phase, and the other one is a magnetic disorder regime. In the stripe and CSL phase, our DMRG results do not support coexistence of magnetic and topological order. In the magnetic disorder regime, the spin structure factor shows broad peaks at $\mathbf{k} = (0, \pi)$, $(\pi, 0)$ and $(\pm\pi/2, \pm\pi/2)$, which agrees with the spin configuration of the CSS magnetic order. However, finite-size scaling of magnetic order parameters suggests no magnetic ordering in the thermodynamic limit. On the other hand, the entanglement spectrum of the ground state exhibits the quasidegenerate levels that are consistent with the CSL. Therefore, the obtained ground state appears like the vacuum-sector ground state of a CSL. The absent spinon sector in the flux insertion simulation implies that the state corresponding to the ground state in the spinon sector may intersect with higher-energy states. The exact nature of this magnetic disorder regime needs further studies on larger system size or by investigating other properties.

Beyond the phase diagram in Fig. 1, we also study the J_χ -dominant regime. While the spin-1 J_1 - J_2 - J_χ model still possesses the CSS state in this regime, this magnetic order seems to give way to a disordered dimer state in the studied spin-1/2 system due to the stronger quantum fluctuations. Our results show the striking differences between the spin-1/2 and spin-1 systems, and provide numerical insights for further understanding on the coexistence of conventional order and topological order.

Note added. Recently, we became aware of an article by Yang *et al.* [79], who studied the same model by using numerical simulations. Both of the two works consistently find

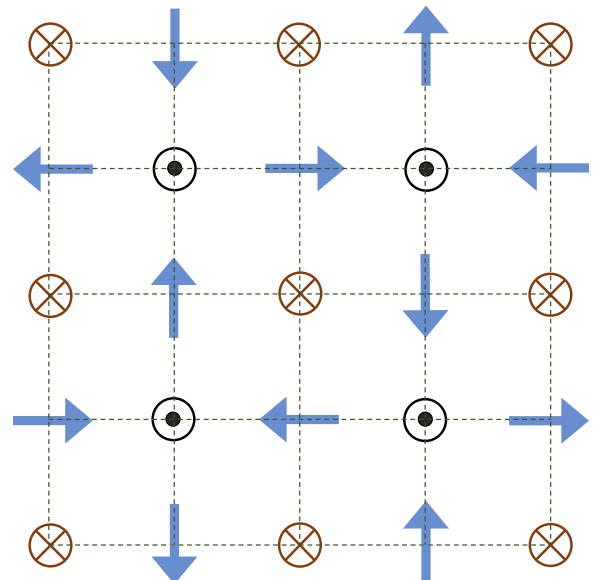


FIG. 11. Spin configuration of the classical magnetic chiral spin state. The arrows denote the spins pointing in the different directions.

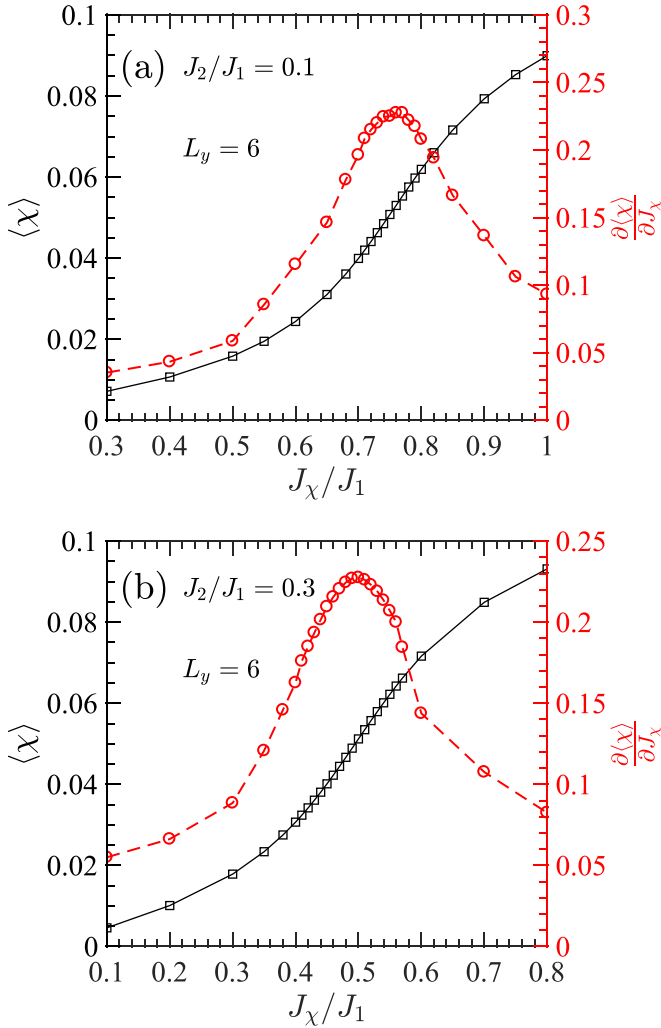


FIG. 12. The bulk chiral order $\langle \chi \rangle$ versus J_x/J_1 and its derivative $\partial \langle \chi \rangle / \partial J_x$ for $J_2/J_1 = 0.1$ and 0.3 on the $L_y = 6$ systems.

the Néel AFM, stripe AFM, chiral spin liquid, and magnetic disorder (called the nematic spin liquid in their paper) phases. While Ref. [79] proposes a magnetically ordered chiral spin state based on the enhanced spin structure factor, our finite-size extrapolation results suggest that the chiral spin state is unlikely in the studied parameter regime.

ACKNOWLEDGMENTS

We acknowledge the stimulating discussions with Jian-Wei Yang, Wei Zhu, and Ling Wang. X.T.Z. and S.S.G. were supported by the National Natural Science Foundation of China (Grants No. 11874078 and No. 11834014) and the Special Project in Key Areas for General Universities in Guangdong Province (Project No. 2023ZDZX3054). Y.H. was supported by the U.S. DOE NNSA under Contract No. 89233218CNA000001 and by the Center for Integrated Nanotechnologies, a DOE BES user facility, in partnership with the LANL Institutional Computing Program for computational resources. H.Q.W. was supported by Guangdong Provincial Key Laboratory of Magnetoelectric Physics and Devices (Grant No. 2022B1212010008) and

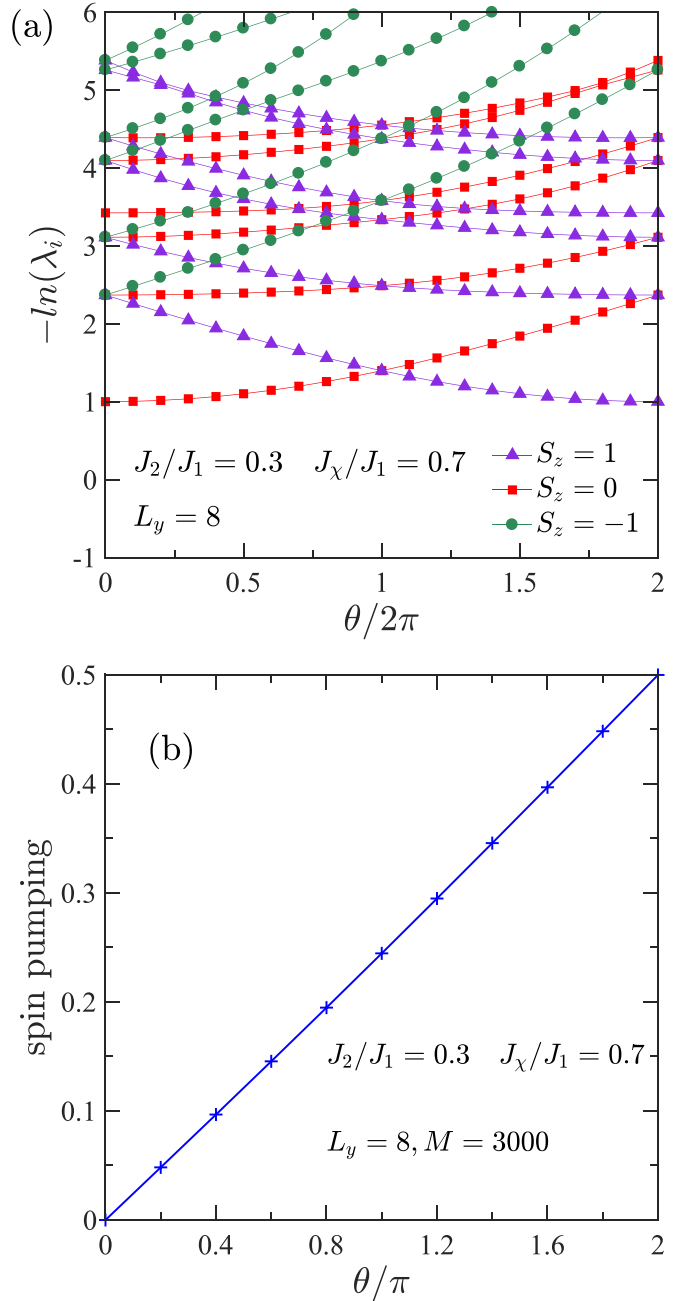


FIG. 13. Adiabatic flux insertion simulation and quantized spin Chern number for $J_2/J_1 = 0.3$, $J_x/J_1 = 0.7$ on the $L_y = 8$ cylinder. (a) Entanglement spectrum flow with adiabatically inserted flux θ , which is obtained by iDMRG simulation with 1000 bond dimensions. The eigenvalues in the $S_z = 0, \pm 1$ sectors are labeled by different symbols. (b) Spin pumping with adiabatically inserted flux θ , which is obtained by iDMRG simulation with 3000 bond dimensions. In a period of inserted flux $\theta = 0 \rightarrow 2\pi$, a quantized magnetization moment 0.5 is accumulated at one open boundary of the cylinder, indicating a fractionally quantized spin Chern number $C = 1/2$.

Guangzhou Basic and Applied Basic Research Foundation (Grant No. 202201011569). D.N.S. was supported by the National Science Foundation through the Partnership in Research and Education in Materials Grant No. DMR-1828019.

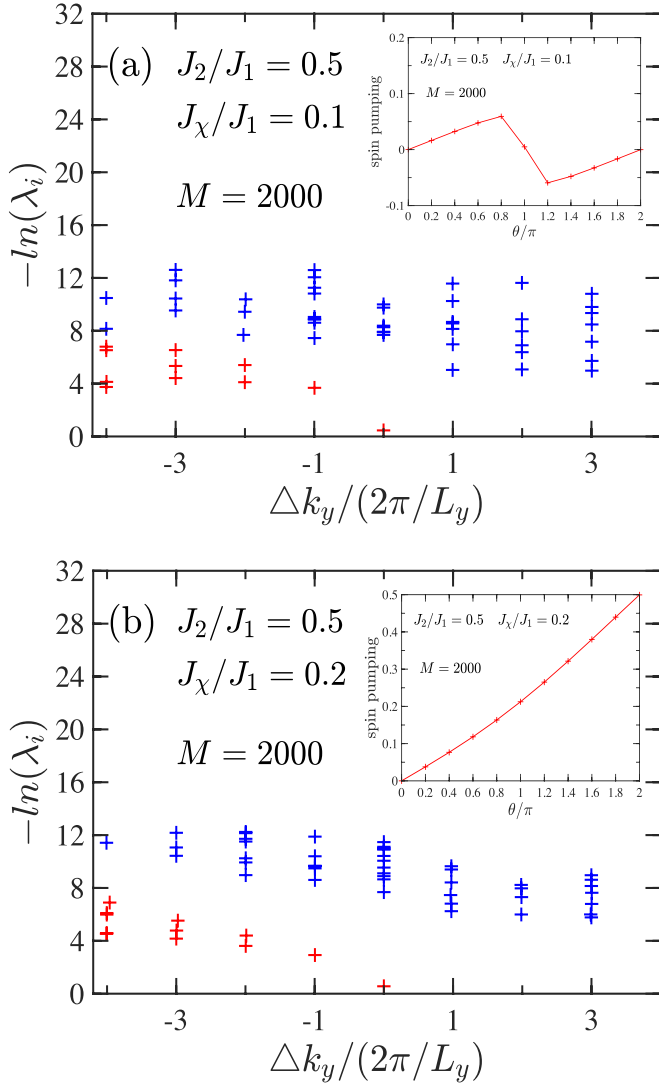


FIG. 14. Entanglement spectrum and adiabatic flux insertion simulations in the intermediate J_2/J_1 regime. [(a) and (b)] The entanglement spectrum labeled by the quantum numbers of total spin $S^z = 0$ and relative momentum along the y direction, Δk_y , for the ground states of $J_2/J_1 = 0.5$, $J_\chi/J_1 = 0.1$ and 0.2 , respectively, on the $L_y = 8$ cylinder systems. λ_i are the eigenvalues of reduced density matrix. The results are obtained by keeping 2000 U(1) states. The insets show the spin pumping with adiabatically inserted flux θ . The results at $J_\chi/J_1 = 0.2$ characterize the ground state as the CSL state.

S.S.G. and H.Q.W. also acknowledge the support from the Dongguan Key Laboratory of Artificial Intelligence Design for Advanced Materials.

APPENDIX A: MAGNETICALLY ORDERED CHIRAL SPIN STATE

To demonstrate the magnetic chiral spin state (CSS), we plot the spin configuration of the classical CSS in Fig. 11, where the different arrows denote the spins pointing in the different directions. One can find that the spin configuration has the translation period of 4 along both the x and y

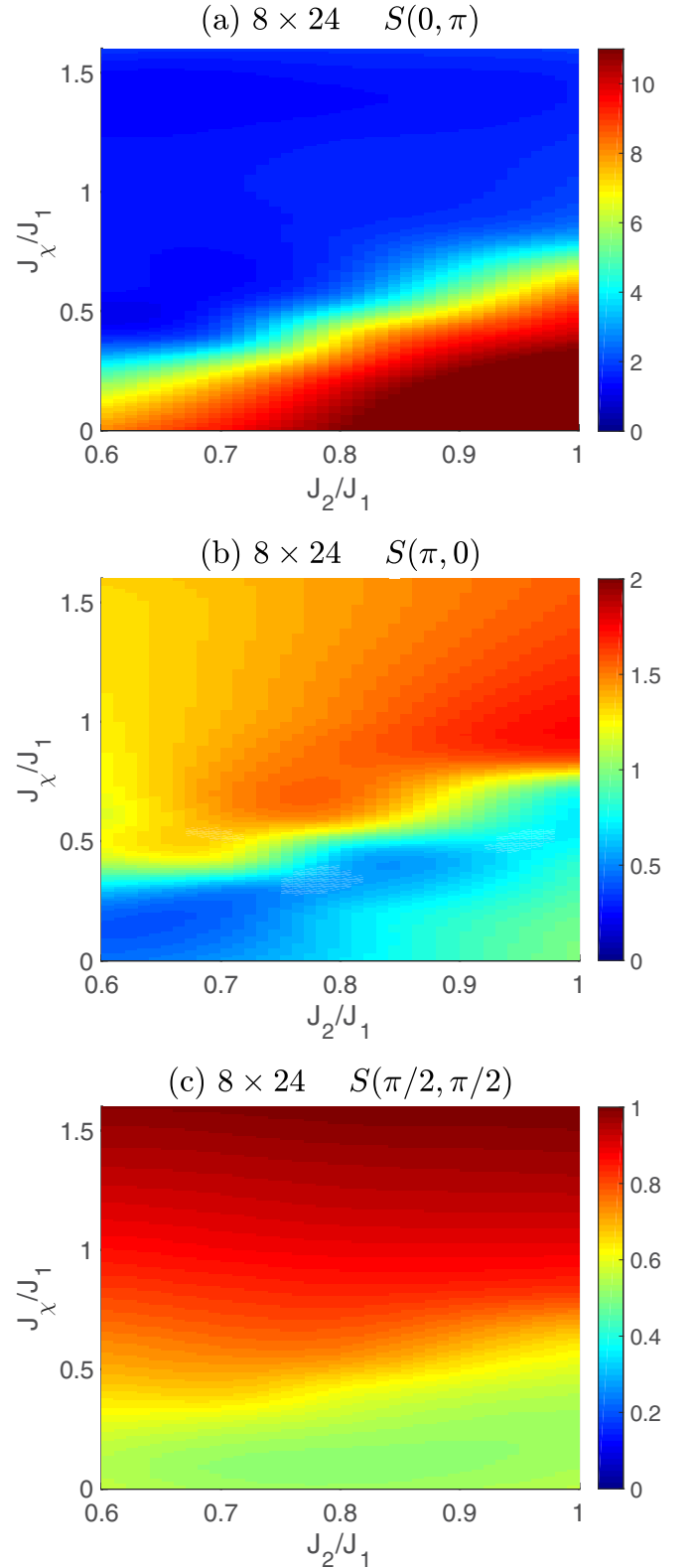


FIG. 15. Coupling dependence of spin structure factors on the eight-leg systems. Results for (a) $S(0, \pi)$, (b) $S(\pi, 0)$, and (c) $S(\pi/2, \pi/2)$.

directions. Classically, the square-lattice system with only the three-spin scalar chiral interaction $J_\chi \mathbf{S}_i \cdot (\mathbf{S}_j \times \mathbf{S}_k)$ can lead to this CSS.

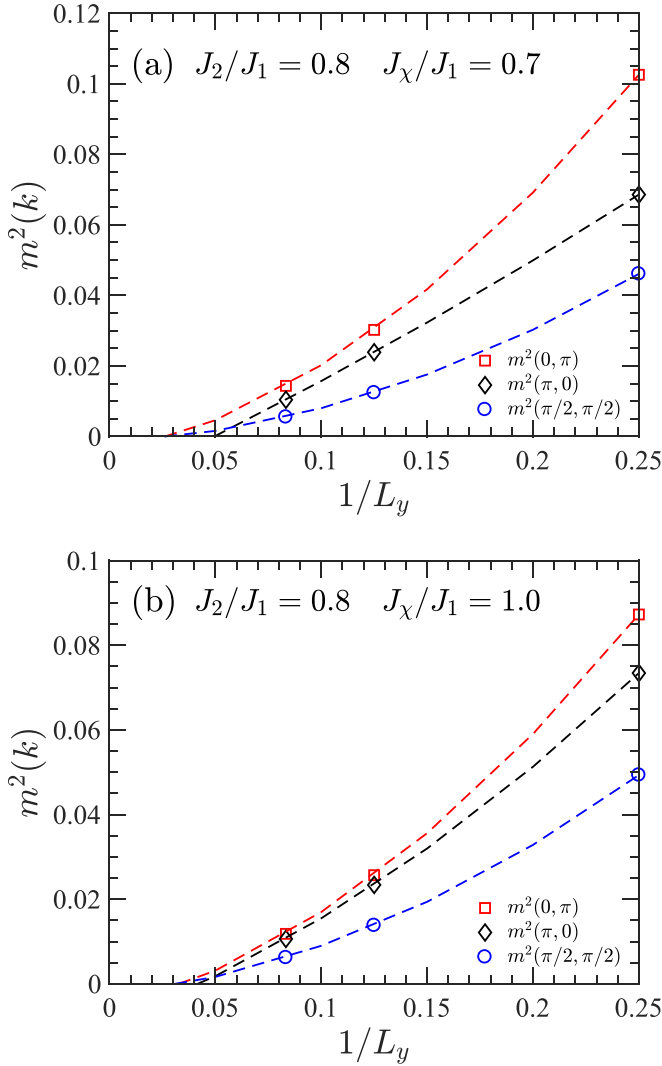


FIG. 16. Finite-size scaling of the magnetic order parameters $m^2(0, \pi)$, $m^2(\pi, 0)$, and $m^2(\pi/2, \pi/2)$ on the $L_y = 4, 8, 12$ systems for (a) $J_2/J_1 = 0.8$, $J_x/J_1 = 0.7$, and (b) $J_2/J_1 = 0.8$, $J_x/J_1 = 1.0$. The results for $L_y = 12$ are obtained by keeping 4000 SU(2) multiplets.

In the quantum case, the spin-1 square-lattice J_1 - J_2 - J_x model has been studied by DMRG calculation [60], which focuses on the intermediate $0.4 \leq J_2/J_1 \leq 0.6$. In this region, a relatively small chiral coupling $J_x/J_1 \gtrsim 0.4$ can induce a robust CSS magnetic order [60].

APPENDIX B: MORE DATA ABOUT PHASE TRANSITION

In Fig. 2 of the main text, we have shown the DMRG results for determining the transition with vanishing Néel AFM order at $J_2 = 0$. Here, we demonstrate more DMRG data to support the similar transition with increasing J_x at finite J_2 in Fig. 12, where the derivative of the bulk chiral order $\langle \chi \rangle$ with respect to J_x/J_1 clearly characterizes the phase transition.

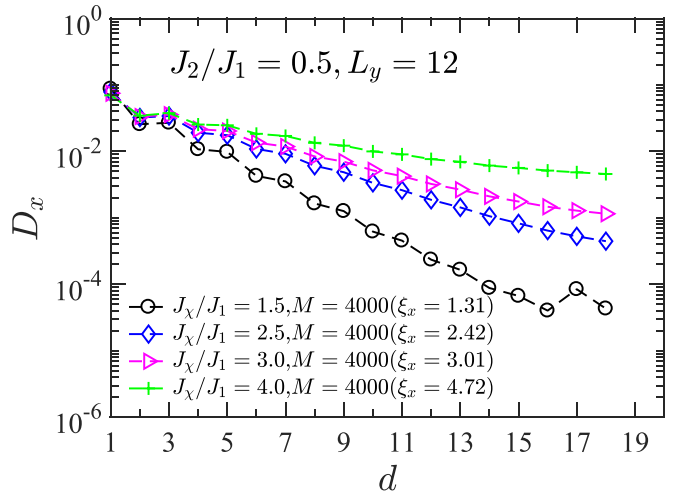


FIG. 17. Log-linear plot of the horizontal dimer order parameter D_x versus the distance d for $J_2/J_1 = 0.5$ and different J_x/J_1 on the $L_y = 12$ cylinder. d is the distance of the bond from the open edge. The exponential fitting of $D_x \sim e^{-d/\xi_x}$ gives the decay length ξ_x . The results are obtained by keeping 4000 SU(2) multiplets.

APPENDIX C: MORE DATA OF ENTANGLEMENT SPECTRUM AND ADIABATIC FLUX INSERTION RESULTS IN THE CHIRAL SPIN LIQUID PHASE

In Figs. 3 and 4 of the main text, we have shown the DMRG results to identify the CSL state at $J_x/J_1 = 1.0$, $J_2 = 0$. Here, we demonstrate additional DMRG data to support the CSL phase at $J_2 \neq 0$ in Fig. 13, for $J_2/J_1 = 0.3$, $J_x/J_1 = 0.7$ on the $L_y = 8$ cylinder. The entanglement spectrum versus flux and the quantized spin Chern number $C = 1/2$ identify the CSL state with double-degenerate ground states.

In the intermediate $J_2/J_1 \simeq 0.5$ regime, the J_1 - J_2 model is a nonmagnetic state [76]. With growing chiral coupling, we find that the system will be easily driven to the CSL phase by a small chiral coupling. In Fig. 14, we show the entanglement spectrum and adiabatic flux insertion results for $J_2/J_1 = 0.5$, $J_x/J_1 = 0.1$ and 0.2 . While the DMRG results at $J_x/J_1 = 0.1$ do not support a CSL, the CSL evidence is robust at $J_x/J_1 = 0.2$. By using similar simulations, we identify the CSL state in the intermediate J_2/J_1 regime with a small chiral coupling, as shown in Fig. 1.

APPENDIX D: ANALYSES OF MAGNETIC ORDER PARAMETERS

In order to explore a possible weak CSS magnetic order in the magnetic disorder regime shown in Fig. 1, we have studied spin structure factors $S(0, \pi)$, $S(\pi, 0)$, and $S(\pi/2, \pi/2)$ for $0.6 \leq J_2/J_1 \leq 1.0$ and $0 \leq J_x/J_1 \leq 1.5$ on the $L_y = 8$ cylinder, as shown in Fig. 15. In Fig. 15(a), $S(0, \pi)$ generally becomes weaker with increased chiral coupling. While $S(0, \pi)$ is strongly suppressed with vanishing stripe magnetic order, $S(\pi, 0)$ shows a relatively stronger intensity for $0.8 \lesssim J_2/J_1 \lesssim 1.0$ and $0.7 \lesssim J_x/J_1 \lesssim 1.3$ as shown in Fig. 15(b). Notice that in this parameter region, $S(0, \pi)$ and $S(\pi, 0)$ have similar magnitudes. On the contrary, as demonstrated

in Fig. 15(c), $S(\pi/2, \pi/2)$ is slightly enhanced with increased chiral coupling, in particular when the stripe order is suppressed.

To make finite-size scaling for magnetic order parameters, we choose three parameter points in the region where the spin structure factors $S(0, \pi)$, $S(\pi, 0)$, and $S(\pi/2, \pi/2)$ are all relatively strong on the eight-leg system. In Fig. 8, we have shown the finite-size scaling of magnetic order parameters at $J_2/J_1 = J_\chi/J_1 = 1.0$. Here, we show the results for $J_2/J_1 = 0.8$, $J_\chi/J_1 = 0.7, 1.0$ in Fig. 16. Similar to the results in Fig. 8, the finite-size scaling of the magnetic order parameters in Fig. 16 decays fast with system width and is smoothly extrapolated to vanished, indicating the absent magnetic order.

APPENDIX E: COUPLING DEPENDENCE OF THE DIMER ORDER DECAY LENGTH

In Fig. 10, we show the log-linear plot of the horizontal dimer order parameter D_x for the pure J_χ model on different system widths, which demonstrates a strong tendency of the system to develop a bond dimer order.

Here, we supplement the results at $J_2/J_1 = 0.5$ with different J_χ couplings on the $L_y = 12$ cylinder. As shown in Fig. 17, the decay length ξ_x of the dimer order parameter D_x keeps growing with increased chiral coupling, which consistently suggests the stronger tendency to develop a dimer order at larger chiral coupling.

-
- [1] L. Savary and L. Balents, Quantum spin liquids: A review, *Rep. Prog. Phys.* **80**, 016502 (2017).
- [2] Y. Zhou, K. Kanoda, and T.-K. Ng, Quantum spin liquid states, *Rev. Mod. Phys.* **89**, 025003 (2017).
- [3] C. Broholm, R. J. Cava, S. A. Kivelson, D. G. Nocera, M. R. Norman, and T. Senthil, Quantum spin liquids, *Science* **367**, eaay0668 (2020).
- [4] T. Lancaster, Quantum spin liquids, *Contemp. Phys.* **64**, 127 (2023).
- [5] S. Kivelson and S. Sondhi, 50 years of quantum spin liquids, *Nat. Rev. Phys.* **5**, 368 (2023).
- [6] X.-G. Wen, Topological orders in rigid states, *Int. J. Mod. Phys. B* **04**, 239 (1990).
- [7] X. G. Wen, Mean-field theory of spin-liquid states with finite energy gap and topological orders, *Phys. Rev. B* **44**, 2664 (1991).
- [8] T. Senthil and M. P. A. Fisher, Z_2 gauge theory of electron fractionalization in strongly correlated systems, *Phys. Rev. B* **62**, 7850 (2000).
- [9] T. Senthil and M. P. A. Fisher, Fractionalization in the cuprates: Detecting the topological order, *Phys. Rev. Lett.* **86**, 292 (2001).
- [10] X. Chen, Z.-C. Gu, and X.-G. Wen, Local unitary transformation, long-range quantum entanglement, wave function renormalization, and topological order, *Phys. Rev. B* **82**, 155138 (2010).
- [11] V. Kalmeyer and R. B. Laughlin, Equivalence of the resonating-valence-bond and fractional quantum Hall states, *Phys. Rev. Lett.* **59**, 2095 (1987).
- [12] X. G. Wen, F. Wilczek, and A. Zee, Chiral spin states and superconductivity, *Phys. Rev. B* **39**, 11413 (1989).
- [13] G. Baskaran, Novel local symmetries and chiral-symmetry-broken phases in $S = 1/2$ triangular-lattice Heisenberg model, *Phys. Rev. Lett.* **63**, 2524 (1989).
- [14] K. Yang, L. K. Warman, and S. M. Girvin, Possible spin-liquid states on the triangular and kagomé lattices, *Phys. Rev. Lett.* **70**, 2641 (1993).
- [15] F. D. M. Haldane and D. P. Arovas, Quantized spin currents in two-dimensional chiral magnets, *Phys. Rev. B* **52**, 4223 (1995).
- [16] D. F. Schroeter, E. Kapit, R. Thomale, and M. Greiter, Spin Hamiltonian for which the chiral spin liquid is the exact ground state, *Phys. Rev. Lett.* **99**, 097202 (2007).
- [17] R. Thomale, E. Kapit, D. F. Schroeter, and M. Greiter, Parent Hamiltonian for the chiral spin liquid, *Phys. Rev. B* **80**, 104406 (2009).
- [18] M. Greiter, D. F. Schroeter, and R. Thomale, Parent Hamiltonian for the non-Abelian chiral spin liquid, *Phys. Rev. B* **89**, 165125 (2014).
- [19] F. Wilczek, *Fractional Statistics and Anyon Superconductivity* (World Scientific, Singapore, 1990), Vol. 5.
- [20] Y.-C. He, D. N. Sheng, and Y. Chen, Chiral spin liquid in a frustrated anisotropic kagome Heisenberg model, *Phys. Rev. Lett.* **112**, 137202 (2014).
- [21] S.-S. Gong, W. Zhu, and D. N. Sheng, Emergent chiral spin liquid: Fractional quantum Hall effect in a kagome Heisenberg model, *Sci. Rep.* **4**, 6317 (2014).
- [22] A. Wietek, A. Sterdyniak, and A. M. Läuchli, Nature of chiral spin liquids on the kagome lattice, *Phys. Rev. B* **92**, 125122 (2015).
- [23] W.-J. Hu, W. Zhu, Y. Zhang, S. Gong, F. Becca, and D. N. Sheng, Variational Monte Carlo study of a chiral spin liquid in the extended Heisenberg model on the kagome lattice, *Phys. Rev. B* **91**, 041124(R) (2015).
- [24] S.-S. Gong, W. Zhu, L. Balents, and D. N. Sheng, Global phase diagram of competing ordered and quantum spin-liquid phases on the kagome lattice, *Phys. Rev. B* **91**, 075112 (2015).
- [25] C. Hickey, L. Cincio, Z. Papić, and A. Paramekanti, Emergence of chiral spin liquids via quantum melting of noncoplanar magnetic orders, *Phys. Rev. B* **96**, 115115 (2017).
- [26] S.-S. Gong, W. Zhu, J.-X. Zhu, D. N. Sheng, and K. Yang, Global phase diagram and quantum spin liquids in a spin- $\frac{1}{2}$ triangular antiferromagnet, *Phys. Rev. B* **96**, 075116 (2017).
- [27] A. Wietek and A. M. Läuchli, Chiral spin liquid and quantum criticality in extended $S = \frac{1}{2}$ Heisenberg models on the triangular lattice, *Phys. Rev. B* **95**, 035141 (2017).
- [28] A. E. B. Nielsen, G. Sierra, and J. I. Cirac, Local models of fractional quantum Hall states in lattices and physical implementation, *Nat. Commun.* **4**, 2864 (2013).
- [29] D. Poilblanc, Investigation of the chiral antiferromagnetic Heisenberg model using projected entangled pair states, *Phys. Rev. B* **96**, 121118(R) (2017).
- [30] J.-Y. Chen, J.-W. Li, P. Nataf, S. Capponi, M. Mambrini, K. Totsuka, H.-H. Tu, A. Weichselbaum, J. von Delft, and D. Poilblanc, Abelian $SU(N)_1$ chiral spin liquids on the square lattice, *Phys. Rev. B* **104**, 235104 (2021).
- [31] J. Hasik, M. Van Damme, D. Poilblanc, and L. Vanderstraeten, Simulating chiral spin liquids with projected entangled-pair states, *Phys. Rev. Lett.* **129**, 177201 (2022).

- [32] A. Szasz, J. Motruk, M. P. Zaletel, and J. E. Moore, Chiral spin liquid phase of the triangular lattice Hubbard model: A density matrix renormalization group study, *Phys. Rev. X* **10**, 021042 (2020).
- [33] C. Boos, C. J. Ganahl, M. Lajkó, P. Nataf, A. M. Läuchli, K. Penc, K. P. Schmidt, and F. Mila, Time-reversal symmetry breaking Abelian chiral spin liquid in Mott phases of three-component fermions on the triangular lattice, *Phys. Rev. Res.* **2**, 023098 (2020).
- [34] A. Szasz and J. Motruk, Phase diagram of the anisotropic triangular lattice Hubbard model, *Phys. Rev. B* **103**, 235132 (2021).
- [35] T. Cookmeyer, J. Motruk, and J. E. Moore, Four-spin terms and the origin of the chiral spin liquid in Mott insulators on the triangular lattice, *Phys. Rev. Lett.* **127**, 087201 (2021).
- [36] B.-B. Chen, Z. Chen, S.-S. Gong, D. N. Sheng, W. Li, and A. Weichselbaum, Quantum spin liquid with emergent chiral order in the triangular-lattice Hubbard model, *Phys. Rev. B* **106**, 094420 (2022).
- [37] Y.-F. Jiang and H.-C. Jiang, Topological superconductivity in the doped chiral spin liquid on the triangular lattice, *Phys. Rev. Lett.* **125**, 157002 (2020).
- [38] Y. Huang and D. N. Sheng, Topological chiral and nematic superconductivity by doping Mott insulators on triangular lattice, *Phys. Rev. X* **12**, 031009 (2022).
- [39] Y. Huang, S.-S. Gong, and D. N. Sheng, Quantum phase diagram and spontaneously emergent topological chiral superconductivity in doped triangular-lattice Mott insulators, *Phys. Rev. Lett.* **130**, 136003 (2023).
- [40] G. Grissonnanche, A. Legros, S. Badoux, E. Lefrançois, V. Zlatko, M. Lizaie, F. Laliberté, A. Gourgout, J.-S. Zhou, S. Pyon, T. Takayama, H. Takagi, S. Ono, N. Doiron-Leyraud, and L. Taillefer, Giant thermal Hall conductivity in the pseudogap phase of cuprate superconductors, *Nature (London)* **571**, 376 (2019).
- [41] G. Grissonnanche, S. Thériault, A. Gourgout, M.-E. Boulanger, E. Lefrançois, A. Ataei, F. Laliberté, M. Dion, J.-S. Zhou, S. Pyon *et al.*, Chiral phonons in the pseudogap phase of cuprates, *Nat. Phys.* **16**, 1108 (2020).
- [42] M.-E. Boulanger, G. Grissonnanche, S. Badoux, A. Allaire, É. Lefrançois, A. Legros, A. Gourgout, M. Dion, C. H. Wang, X. H. Chen *et al.*, Thermal Hall conductivity in the cuprate Mott insulators Nd_2CuO_4 and $\text{Sr}_2\text{CuO}_2\text{Cl}_2$, *Nat. Commun.* **11**, 5325 (2020).
- [43] M.-E. Boulanger, G. Grissonnanche, É. Lefrançois, A. Gourgout, K.-J. Xu, Z.-X. Shen, R. L. Greene, and L. Taillefer, Thermal Hall conductivity of electron-doped cuprates, *Phys. Rev. B* **105**, 115101 (2022).
- [44] M.-E. Boulanger, L. Chen, V. Oliviero, D. Vignolles, G. Grissonnanche, K. Xu, Z.-X. Shen, C. Proust, J. Baglo, and L. Taillefer, Thermal Hall conductivity of electron-doped cuprates: Electrons and phonons, [arXiv:2310.15892](https://arxiv.org/abs/2310.15892).
- [45] R. Samajdar, M. S. Scheurer, S. Chatterjee, H. Guo, C. Xu, and S. Sachdev, Enhanced thermal Hall effect in the square-lattice Néel state, *Nat. Phys.* **15**, 1290 (2019).
- [46] R. Samajdar, S. Chatterjee, S. Sachdev, and M. S. Scheurer, Thermal Hall effect in square-lattice spin liquids: A Schwinger boson mean-field study, *Phys. Rev. B* **99**, 165126 (2019).
- [47] J. H. Han, J.-H. Park, and P. A. Lee, Consideration of thermal Hall effect in undoped cuprates, *Phys. Rev. B* **99**, 205157 (2019).
- [48] Z.-X. Li and D.-H. Lee, The thermal Hall conductance of two doped symmetry-breaking topological insulators, [arXiv:1905.04248](https://arxiv.org/abs/1905.04248).
- [49] T. Li, Theory of the giant thermal Hall effect in the high temperature superconductors, [arXiv:1906.01712](https://arxiv.org/abs/1906.01712).
- [50] Y. Zhang, Y. Teng, R. Samajdar, S. Sachdev, and M. S. Scheurer, Phonon Hall viscosity from phonon-spinon interactions, *Phys. Rev. B* **104**, 035103 (2021).
- [51] J. Merino and A. Ralko, Majorana chiral spin liquid in a model for Mott insulating cuprates, *Phys. Rev. Res.* **4**, 023122 (2022).
- [52] C. M. Varma, Thermal Hall effect in the pseudogap phase of cuprates, *Phys. Rev. B* **102**, 075113 (2020).
- [53] H. Guo and S. Sachdev, Extrinsic phonon thermal Hall transport from Hall viscosity, *Phys. Rev. B* **103**, 205115 (2021).
- [54] M. Ye, L. Savary, and L. Balents, Phonon Hall viscosity in magnetic insulators, [arXiv:2103.04223](https://arxiv.org/abs/2103.04223).
- [55] L. Mangeolle, L. Balents, and L. Savary, Phonon thermal Hall conductivity from scattering with collective fluctuations, *Phys. Rev. X* **12**, 041031 (2022).
- [56] L. Mangeolle, L. Balents, and L. Savary, Thermal conductivity and theory of inelastic scattering of phonons by collective fluctuations, *Phys. Rev. B* **106**, 245139 (2022).
- [57] B. Flebus and A. H. MacDonald, Charged defects and phonon Hall effects in ionic crystals, *Phys. Rev. B* **105**, L220301 (2022).
- [58] X.-Q. Sun, J.-Y. Chen, and S. A. Kivelson, Large extrinsic phonon thermal Hall effect from resonant scattering, *Phys. Rev. B* **106**, 144111 (2022).
- [59] X.-J. Liu, Z.-X. Liu, K. T. Law, W. V. Liu, and T. K. Ng, Chiral topological orders in an optical Raman lattice, *New J. Phys.* **18**, 035004 (2016).
- [60] Y. Huang, W. Zhu, S.-S. Gong, H.-C. Jiang, and D. N. Sheng, Coexistence of non-Abelian chiral spin liquid and magnetic order in a spin-1 antiferromagnet, *Phys. Rev. B* **105**, 155104 (2022).
- [61] D. A. Rabson and S. A. Trugman, A spin model for investigating chirality, *J. Phys.: Condens. Matter* **7**, 9005 (1995).
- [62] S. R. White, Density matrix formulation for quantum renormalization groups, *Phys. Rev. Lett.* **69**, 2863 (1992).
- [63] I. P. McCulloch and M. Gulácsi, The non-Abelian density matrix renormalization group algorithm, *Europhys. Lett.* **57**, 852 (2002).
- [64] J. Hauschild and F. Pollmann, Efficient numerical simulations with Tensor Networks: Tensor Network Python (TeNPy), *SciPost Phys. Lect. Notes*, **5** (2018), code available from <https://github.com/tenpy/tenpy>.
- [65] S. Yan, D. A. Huse, and S. R. White, Spin-liquid ground state of the $S = 1/2$ kagome Heisenberg antiferromagnet, *Science* **332**, 1173 (2011).
- [66] H.-C. Jiang, Z. Wang, and L. Balents, Identifying topological order by entanglement entropy, *Nat. Phys.* **8**, 902 (2012).
- [67] J. Eisert, M. Cramer, and M. B. Plenio, Colloquium: Area laws for the entanglement entropy, *Rev. Mod. Phys.* **82**, 277 (2010).
- [68] A. Kitaev and J. Preskill, Topological entanglement entropy, *Phys. Rev. Lett.* **96**, 110404 (2006).
- [69] M. Levin and X.-G. Wen, Detecting topological order in a ground state wave function, *Phys. Rev. Lett.* **96**, 110405 (2006).
- [70] H. Li and F. D. M. Haldane, Entanglement spectrum as a generalization of entanglement entropy: Identification of topological

- order in non-Abelian fractional quantum Hall effect states, *Phys. Rev. Lett.* **101**, 010504 (2008).
- [71] X.-L. Qi, H. Katsura, and A. W. W. Ludwig, General relationship between the entanglement spectrum and the edge state spectrum of topological quantum states, *Phys. Rev. Lett.* **108**, 196402 (2012).
- [72] L. Cincio and G. Vidal, Characterizing topological order by studying the ground states on an infinite cylinder, *Phys. Rev. Lett.* **110**, 067208 (2013).
- [73] M. P. Zaletel, R. S. K. Mong, and F. Pollmann, Topological characterization of fractional quantum Hall ground states from microscopic Hamiltonians, *Phys. Rev. Lett.* **110**, 236801 (2013).
- [74] P. Di Francesco, P. Mathieu, and D. Senechal, *Conformal Field Theory*, Graduate Texts in Contemporary Physics (Springer-Verlag, New York, 1997).
- [75] Y. Hatsugai, Chern number and edge states in the integer quantum Hall effect, *Phys. Rev. Lett.* **71**, 3697 (1993).
- [76] W.-Y. Liu, S.-S. Gong, Y.-B. Li, D. Poilblanc, W.-Q. Chen, and Z.-C. Gu, Gapless quantum spin liquid and global phase diagram of the spin-1/2 J_1 - J_2 square antiferromagnetic Heisenberg model, *Sci. Bull.* **67**, 1034 (2022).
- [77] A. W. Sandvik, Finite-size scaling and boundary effects in two-dimensional valence-bond solids, *Phys. Rev. B* **85**, 134407 (2012).
- [78] S.-S. Gong, W. Zhu, D. N. Sheng, O. I. Motrunich, and M. P. A. Fisher, Plaquette ordered phase and quantum phase diagram in the spin- $\frac{1}{2}$ J_1 - J_2 square Heisenberg model, *Phys. Rev. Lett.* **113**, 027201 (2014).
- [79] J. Yang, Z. Liu, and L. Wang, Ground state phase diagram and the exotic phases in the spin-1/2 square lattice J_1 - J_2 - J_χ model, [arXiv:2401.03434](https://arxiv.org/abs/2401.03434).